Clays and Clay Minerals, Vol. 65, No. 4, 234–251, 2017.

CRYSTAL-CHEMICAL REGULARITIES AND IDENTIFICATION CRITERIA IN Fe-BEARING, K-DIOCTAHEDRAL 1*M* MICAS FROM X-RAY DIFFRACTION AND INFRARED SPECTROSCOPY DATA

Bella B. Zviagina[1,*], Victor A. Drits[1], Boris A. Sakharov[1], Tatiana A. Ivanovskaya[1], Olga V. Dorzhieva[1,2], and Douglas K. McCarty[3]

[1] Geological Institute of the Russian Academy of Science, Pyzhevsky per. 7, 119017 Moscow, Russia
[2] Institute of Ore Deposits, Petrography, Mineralogy, and Geochemistry of the Russian Academy of Science, Staromonetny per. 35, 7, 119017 Moscow, Russia
[3] Institute of Geological Sciences, Polish Academy of Sciences – Research Centre in Krakow, ul. Senacka 1, 31-002 Krakow, Poland

Abstract—Iron-bearing K-dioctahedral 1*M* and 1*M*d micas are abundant in diverse geological environments and vary in composition from illite to celadonite through Fe-illite, Al-glauconite, and glauconite. The chemistry and structural features of these micas are complex and heterogeneous, reliable diagnostic criteria are lacking, and the conventional mineralogical nomenclature is ambiguous, which complicate the identification of these mica varieties. The objectives of the present study were to reveal the structural and crystal-chemical variability in Fe-bearing, K-dioctahedral 1*M* micas and to define composition ranges and identification criteria for the mica varieties in the series. A collection of samples of various compositions was studied using X-ray diffraction (XRD) and Fourier-transform infrared (FTIR) spectroscopy. Analysis of the relationships between unit-cell parameters and cation composition showed that the series included four groups, namely, Fe-bearing illites, Al-glauconites, glauconites, and celadonites and each group was characterized by a specific combination of unit-cell parameters and variation ranges. The illite group contained two distinct subgroups; Fe-bearing, Mg-rich illites and Fe-illites; which differ in the range of cation compositions and in FTIR characteristics. The boundary between Fe-illites and Al-glauconites occurs at a unit cell *b* value of ~9.05 Å and at ratios of octahedral Al to total trivalent octahedral cations that range between 0.60 and 0.65. The partially overlapping cation composition and cell parameter ranges may complicate the distinction between Al-glauconites and glauconites, which can still be unambiguously differentiated using FTIR data. The dramatically different XRD and FTIR characteristics confirmed that glauconite and celadonite should be treated as separate mineral species. The distinctive features of celadonite are relatively low $c\sin\beta$ values and reduced $|c\cos\beta/a|$ values combined with *b* parameters lower than glauconites, but similar to Fe-illites. Celadonites also have distinct and sharp FTIR absorption bands at specific positions in the Si-O and OH stretching regions.

Key Words—Celadonite, Dioctahedral Mica, FTIR Spectroscopy, Glauconite, Illite, Unit-cell Parameters, X-ray Diffraction.

INTRODUCTION

Isomorphous cation substitutions in the tetrahedral and octahedral sheets typical for micas in general are especially diverse in low-temperature, K-dioctahedral micas. Conventionally, two isomorphous series are distinguished among low-temperature, K-dioctahedral micas and micaceous minerals, which normally occur as 1*M* and 1*Md* polytypes: (a) Al-rich, Fe-poor varieties from (Mg, Fe)-poor illite to aluminoceladonite through Mg-rich illite and (b) Fe-rich varieties from glauconite to celadonite (Środoń and Eberl, 1984; Drits and Kossovskaya, 1991; Brigatti and Guggenheim, 2002; Drits *et al.*, 2006, 2010; Wilson, 2013; Zviagina *et al.*, 2015). In addition to compositional variations, the 1*M* K-dioctahedral micas display a structural diversity that is associated with the different patterns in the distribution of octahedral cations over the available structural positions. Al-rich, K-dioctahedral micas may consist of either *trans*-vacant (*tv*) or *cis*-vacant (*cv*) 2:1 layers or interstratified layer types, and the Fe-rich varieties normally have *tv* structures (Drits, 2003; Drits *et al.* 2006, 2010; Drits and Zviagina, 2009). Drits *et al.* (1993a) and Zviagina *et al.* (2007) developed XRD criteria to identify *tv* and *cv* mica polytypes and polymorphs. Drits and Zviagina (2009) considered the advantages and limitations of various diffraction and non-diffraction methods used for determining the layer types in clay minerals.

The distinguishing features and identification criteria to be used for micas in the illite-aluminoceladonite series with $\leqslant 0.3$ Fe cations per half-formula unit (p.h.f.u., *i.e.* per $O_{10}(OH)_2$) were treated in detail in the previous paper (Zviagina *et al.*, 2015). Analysis of the relationships between unit-cell parameters and cation composition showed that the series includes three

* E-mail address of corresponding author:
zbella2001@yahoo.com
DOI:10.1346/CCMN.2017.064061

groups, (Mg, Fe)-poor illites, Mg-rich illites, and aluminoceladonites, each characterized by a unique combination of unit-cell parameter and variation ranges. In particular, the aluminoceladonite distinctive features are lower $c\sin\beta$ (9.90−9.92 Å) and $|c\cos\beta/a|$ (0.36−0.37) values combined with *b* parameters (9.00−9.02 Å) which are smaller than in Mg-rich illite (9.02−9.04 Å) and slightly greater than in (Mg, Fe)-poor illites (8.98−9.00 Å). A new approach to interpreting the FTIR spectroscopy data was used that involves new relationships between band positions and cation compositions of (Mg, Fe)-poor illites, Mg-rich illites, and aluminoceladonites and provides additional diagnostic features, such as band positions and profiles in the Si-O bending, Si-O stretching, and OH-stretching vibration ranges. Up until now, however, several aspects of the crystal chemistry, classification, and identification of Fe-rich, K-dioctahedral micas have received little study.

The Mica Subcommittee appointed by the Commission on New Minerals and Mineral Names of the International Mineralogical Association (IMA-CNMMN) defined glauconite as a series name for interlayer-deficient micas with the average composition $K_{0.8}$ $(R(III)_{1.33}$ $R(II)_{0.67})$ $(Si_{3.87}Al_{0.13})$ O_{10} $(OH)_2$ and with the following range in octahedral composition (a tetrahedral compositional range has not been proposed): $^{VI}R(II)/(^{VI}R(II) + {}^{VI}R(III)) \geqslant 0.15$; $^{VI}Al/(\ ^{VI}Al + {}^{VI}Fe(III)) \leqslant 0.5$ (Rieder *et al*., 1998). This formula and composition range, however, fail to adequately cover the complexity and heterogeneity of the chemical composition of glauconites (see, for example, Ivanovskaya *et al*., 2012, 2015; Wilson, 2013, and references therein). In particular, most natural glauconite samples have a much higher Al for Si substitution (0.3−0.4 cations per half-formula unit.) (Odom, 1984; Ivanovskaya *et al*., 1989, 2012, 2015; Wilson, 2013). Moreover, quite a few mineral samples with compositions that are intermediate between illite and glauconite as defined by the IMA-CNMMN Mica Subcommittee have been reported with $0.5 < {}^{VI}Al/(\ {}^{VI}Al + {}^{VI}Fe(III)) \leqslant 0.6$ (Longuépée and Cousineau, 2006; Tóth and Weiszburg, 2006; Ivanovskaya *et al*., 2012, 2015, and references therein). Such samples were termed Al-glauconites (Tsipursky and Ivanovskaya, 1988; Ivanovskaya *et al*., 1989, 2012, 2015; Drits and Kossovskaya, 1991).

Celadonite is defined as a true-mica end-member with an ideal formula of $K[Fe(III)\ (Mg, Fe(II))]Si_4O_{10}(OH)_2$ along with the more exotic species of ferro-aluminoceladonite $K[Al\ (Fe(II), Mg)]Si_4O_{10}(OH)_2$ and ferroceladonite $K[Fe(III)\ (Fe(II), Mg)]Si_4O_{10}(OH)_2$ (Rieder *et al*., 1998). The octahedral composition range for celadonite proposed by the IMA-CNMMN Mica Subcommittee is $^{VI}R(II)/(\ ^{VI}R(II) + {}^{VI}R(III)) \geqslant 0.25$; $^{VI}Al/(\ ^{VI}Al + {}^{VI}Fe(III)) < 0.5$; $Mg/(Mg + {}^{VI}Fe(II)) > 0.5$. According to this nomenclature, therefore, the range in the octahedral cation composition of glauconite and celadonite overlap, and no clear distinction has been proposed except for the interlayer charge, which is either less than or greater than 0.85 in interlayer deficient micas and true micas, respectively. Whereas no celadonite tetrahedral compositional range has been proposed by the IMA-CNMMN Mica Subcommittee, a previous nomenclature set the value of $^{IV}Al = 0.2$ cation p.h.f.u. as the boundary between celadonite and glauconite (Bailey, 1980). Several authors have supposed that a complete solid solution series exists between glauconite and celadonite (Velde, 1985; Parron and Amouric, 1990; Duplay and Buatier, 1997; Meunier and El-Abani, 2000; Weiszburg *et al*., 2006). Because glauconite does not represent a true end-member species, the term "compositional series" will be used instead of "solid solution" in the present paper. Buckley *et al*. (1978), however, treated celadonite and glauconite as separate mineral species that can be readily differentiated by powder X-ray diffraction (XRD) and infrared spectroscopy (IR). Celadonites tend to have sharper basal and *hkl* reflections and smaller d(060) values in comparison to glauconites (1.506-1.510 *vs*. 1.512-1.518 Å). The celadonite IR spectra show much sharper absorption bands than glauconite, particularly in the OH-stretching region. While a combination of XRD and IR may indeed in many cases be sufficient to identify celadonite, distinguishing between celadonite and glauconite on this basis may not always be possible (Slonimskaya *et al*., 1986; Wilson, 2013).

Up to now, therefore, the issue of whether or not a complete compositional series occurs from glauconite to celadonite has remained unclear. The purpose of the present work was to resolve this and other uncertainties in the classification and identification of Fe-bearing dioctahedral micas. The specific objectives were (a) to reveal diagnostic structural and crystal-chemical features that would allow a distinction between Fe-bearing illite, Al-glauconite, glauconite, and celadonite, (b) to find out whether a continuous compositional series indeed occurs from illite to glauconite and from glauconite to celadonite, and (c) to define the compositional ranges and identification criteria for these mica varieties. For this purpose, the relationships between unit-cell parameters and cation composition were analyzed and Fourier-transform infrared (FTIR) spectroscopy data were examined for Fe-bearing dioctahedral mica samples with a range in compositions from different environments.

MATERIALS AND METHODS

Samples

The studied samples ranged in composition from (Mg, Fe)-rich illite to celadonite through Al-glauconite and glauconite (see Table 1 for mineral identities, locations, and references to publications that characterize the mineralogy and expandable interlayer contents,

https://doi.org/10.1346/CCMN.2017.064061 Published online by Cambridge University Press

Table 1. Sample description.

#	Sample name	Mineral variety	Expandable layer content, W_s* (%)	Origin and location; Reference
1	60	Illite Mg,Fe-rich	8	Silty shales, Upper Riphean, South Urals, Russia; Ivanovskaya *et al*. (1989), Drits *et al*. (2013)
2	60/3	Illite Mg,Fe-rich	5	Clayey siltstones, Upper Riphean, South Urals, Russia; Ivanovskaya *et al*. (1989), Drits *et al*. (2010)
3	BP	Fe-illite	0	Precambrian deposits of Siberian Platform, Bolshoi Patom; Drits *et al*. (1993b), Muller *et al*. (2000)
4	560/3	Fe-illite	6	Sandstones, Lower Riphean, Olenek Uplift, northern Siberia, Russia; Ivanovskaya *et al*. (1993)
5	553/1	Fe-illite	13	Siltstones, Middle Riphean, Olenek Uplift, northern Siberia, Russia; Ivanovskaya (1994)
6	2076A	Fe-illite	7	Sandstones, Lower Riphean, Olenek Uplift, northern Siberia, Russia; Ivanovskaya *et al*. (1993)
7	575	Fe-illite	14	Sandstones, Middle, Riphean, Olenek Uplift, northern Siberia, Russia; Ivanovskaya (2009)
8	BSH11	Fe-illite	n.d.	Siltstones, Upper Riphean, South Urals, Russia, Zaitseva *et al*. (2008); Ivanovskaya *et al*. (2015)
9	BSH12	Fe-illite	n.d.	Siltstones, Upper Riphean, South Urals, Russia, Zaitseva *et al*. (2008); Ivanovskaya *et al*. (2015)
10	KUL1	Fe-illite	n.d.	Siltstones, Upper Riphean, South Urals, Russia, Zaitseva *et al*. (2008); Ivanovskaya *et al*. (2015)
11	400/3	Al-glauconite	5	Gravelly sandstones, Lower Riphean, Anabar Uplift, northern Siberia, Russia; Ivanovskaya and Tsipursky (1990), Drits *et al*. (2013)
12	556	Al-glauconite	11	Sandstones, Middle Riphean, Olenek Uplift, northern Siberia, Russia; Ivanovskaya *et al*. (2006)
13	KUL2	Al-glauconite	10	Siltstones, Upper Riphean, South Urals, Russia; Zaitseva et al. (2008), Ivanovskaya et al. (2015)
14	551	Al-glauconite	8	Gravelly sandstones, Middle Riphean, Olenek Uplift, northern Siberia, Russia; Ivanovskaya (1994), Drits *et al*. (2013)
15	555A	Al-glauconite	6	Gravelly sandstones, Middle Riphean, Olenek Uplift, northern Siberia, Russia; Ivanovskaya (1994)
16	E8/2	Glauconite	0	Ordovician deposits, North-West Russian Platform; Drits et al. (1993b), Muller *et al*. (2000)
17	402/1	Glauconite	8	Silty shale, Lower Riphean, Anabar Uplift, Russia; Ivanovskaya and Tsipursky (1990), Drits *et al*. (2013)
18	103	Glauconite	6	Glauconitites, Lower Ordovician, Parila, Estonia; this work
19	37/71	Glauconite	4	Glauconitites, Lower Ordovician, Vergale, Latvia; this work
20	37/71A	Glauconite	9	Siltstones, Middle Cambrian, Vergale, Latvia; this work
21	BAB	Glauconite	5	Ordovician deposits, Baltic region, Russia; Shutov *et al*. (1975), Drits *et al*. (1993b, 2010)
22	PILT	Glauconite	3	Ordovician sandstone, Latvia; Nikolaeva (1977), Drits *et al*. (1993b, 2010)
23	68-69	Glauconite	5	Leningrad region, Russia; Nikolaeva (1977), Drits *et al*. (1993b, 2010)
24	G294	Glauconite	n.d.	Ordovician, Sweden; Thompson and Hower (1975)
25	GT6-69	Glauconite	n.d.	Cretaceous, Bornholm Island; Thompson and Hower (1975)
26	GT8-66	Glauconite	n.d.	Cambrian, Wyoming; Thompson and Hower (1975)
27	821-057	Glauconite	n.d.	Greensand, Birmingham, New Jersey, Ward's Natural Science Establishment Inc., Rochester, NY; this work.
28	541	Glauconite	n.d.	Lower Cambrian, East Siberia, Russia; Ivanovskaya *et al*. (2015)
29	79/73	Glauconite	n.d.	Zeolite-free sandstones, the Dnieper river, Ukraine; Murav'ev (1983)
30	372/70	Glauconite	n.d.	Zeolite-free sands, the Tyk-Butak river, Kazakhstan; Murav'ev (1983)
31	TAIH	Celadonite	0	Taiheizan, Akita Prefecture, Japan; Kimbara and Shimoda (1973), Drits *et al*. (2010)
32	69	Celadonite	0	Krivoi Rog mining district, Russia; Lazarenko and Pavlishin (1976), Drits *et al*. (2010)
33	Z1	Celadonite	0	Russia; Malkova (1956), Drits (1987), Drits *et al*. (2010)

* W_s is the proportion of smectite interlayers.

https://doi.org/10.1346/CCMN.2017.064061 Published online by Cambridge University Press

W_s). The chemical compositions and corresponding crystal-chemical formulae (Table 2) for samples 68-69, PILT, BAB, TAIH, 69, and Z1 were taken from Drits *et al.* (2010) and the other sample chemical compositions/crystal formulae, from the respective publications in Table 1. The chemical compositions and crystal chemical formulae of samples 37/71, 37/71a, 103, and 821-057 were produced in this paper. Samples 37/71 and 37/71A

Table 2. Cation compositions per $O_{10}(OH)_2$ of the studied samples.

#	Sample	Tetrahedral		Octahedral				Interlayer			K_{Al}	Al_{total}	Fe_{total}
		Si	Al	Al	Fe(III)	Fe(II)	Mg	K	Ca	Na			
1	60	3.63	0.37	1.32	0.13	0.16	0.46	0.77	0	0.01			
	mica	3.6	0.4	1.32	0.13	0.16	0.44	0.84	0	0	0.91	1.72	0.29
2	60/3	3.65	0.35	1.38	0.13	0.15	0.40	0.75	0.02	0.01			
	mica	3.63	0.37	1.36	0.13	0.16	0.40	0.79	0	0.01	0.91	1.73	0.28
3	BP	3.46	0.54	1.11	0.41	0.13	0.42	0.74	0.06	0.01	0.73	1.65	0.54
4	560/3	3.62	0.38	1.12	0.37	0.20	0.32	0.80	0	0.05			
	mica	3.60	0.40	1.13	0.37	0.20	0.31	0.85	0	0.01	0.75	1.53	0.57
5	553/1	3.57	0.43	1.13	0.5	0.19	0.19	0.69	0.04	0.02			
	mica	3.51	0.49	1.16	0.5	0.19	0.16	0.79	0	0.02	0.69	1.65	0.69
6	2076A	3.68	0.32	1.03	0.55	0.09	0.34	0.69	0.01	0.01			
	mica	3.66	0.34	1.04	0.55	0.09	0.32	0.74	0.0	0.0	0.65	1.38	0.64
7	575	3.70	0.30	1.09	0.50	0.21	0.23	0.64	0	0.01			
	mica	3.65	0.35	1.12	0.50	0.21	0.16	0.74	0	0	0.69	1.47	0.71
8	BSH11	3.71	0.29	1.06	0.36	0.23	0.39	0.74	0.02	0	0.75	1.35	0.59
9	BSH12	3.73	0.27	0.88	0.37	0.37	0.47	0.78	0.02	0	0.70	1.15	0.74
10	KUL1	3.71	0.29	0.99	0.43	0.27	0.37	0.78	0.01	0	0.70	1.28	0.70
11	400/3	3.63	0.37	0.91	0.60	0.20	0.34	0.76	0.01	0.02			
	mica	3.63	0.37	0.91	0.58	0.21	0.34	0.80	0	0	0.60	1.28	0.79
12	556	3.6	0.40	0.91	0.62	0.23	0.25	0.67	0.07	0.02			
	mica	3.6	0.40	0.91	0.59	0.26	0.26	0.75	0.04	0.02	0.61	1.31	0.85
13	KUL2	3.72	0.28	0.86	0.54	0.25	0.39	0.76	0.02	0			
	mica	3.69	0.31	0.86	0.54	0.25	0.38	0.84	0	0	0.61	1.17	0.79
14	551	3.67	0.33	0.85	0.77	0.15	0.22	0.77	0.01	0.02			
	mica	3.67	0.33	0.85	0.76	0.17	0.21	0.83	0	0	0.52	1.18	0.93
15	555A	3.63	0.37	0.77	0.76	0.16	0.34	0.73	0.01	0.02			
	mica	3.63	0.37	0.77	0.74	0.17	0.35	0.78	0	0	0.50	1.14	0.91
16	E8/2	3.65	0.35	0.68	0.79	0.1	0.41	0.78	0.05	0.01	0.46	1.03	0.89
17	402/1	3.80	0.20	0.52	0.78	0.28	0.47	0.74	0	0.04			
	mica	3.80	0.20	0.52	0.76	0.30	0.48	0.81	0	0	0.40	0.72	1.06
18	103	3.67	0.33	0.37	1.15	0.11	0.40	0.74	0	0			
	mica	3.67	0.33	0.37	1.14	0.12	0.39	0.79	0	0	0.24	0.70	1.26
19	37/71	3.57	0.43	0.38	1.15	0.10	0.45	0.72	0.01	0.02	0.25	0.81	1.25
20	37/71A	3.56	0.44	0.64	0.96	0.19	0.28	0.68	0	0.01			
	mica	3.56	0.44	0.64	0.94	0.21	0.27	0.75	0	0	0.40	1.08	1.15
21	BAB	3.58	0.42	0.53	0.94	0.13	0.44	0.76	0.05	0.01			
	mica	3.58	0.42	0.53	0.92	0.14	0.45	0.80	0.04	0.01	0.37	0.95	1.06
22	PILT	3.73	0.27	0.44	0.92	0.22	0.47	0.77	0	0.03	0.32	0.71	1.14
23	68-69	3.73	0.27	0.43	0.92	0.30	0.39	0.80	0.01	0.03			
	mica	3.73	0.27	0.43	0.90	0.32	0.39	0.84	0	0.02	0.32	0.70	1.22
24	G294	3.72	0.28	0.74	0.82	n.d.	0.40	0.67	0.06	0.02	0.47	1.02	0.82
25	GT6-69	3.78	0.22	0.57	0.95	n.d.	0.47	0.69	0.01	0	0.38	0.79	0.95
26	GT8-66	3.60	0.40	0.37	1.26	n.d.	0.32	0.72	0	0.12	0.23	0.77	1.26
27	821-057	3.74	0.26	0.33	1.23	n.d.	0.41	0.68	0.03	0.01	0.22	0.89	1.23
28	541	3.53	0.47	0.68	0.72	0.29	0.40	0.78	0.06	0.01	0.49	1.15	1.01
29	79/73	3.65	0.35	0.37	1.16	0.05	0.44	0.67	0.06	0.01	0.27	0.72	1.21
30	372/70	3.68	0.32	0.51	1.01	0.08	0.40	0.65	0.06	0.02	0.27	0.83	1.09
31	TAIH	3.72	0.28	0.16	1.07	0.10	0.71	0.82	0	0.18	0.13	0.44	1.17
32	69	3.94	0.06	0.06	1.15	0.36	0.41	0.83	0.03	0.01	0.05	0.12	1.51
33	Z1	3.96	0.04	0.05	0.96	0.26	0.73	0.89	0	0.07	0.05	0.09	1.22

Note. Unit-cell parameters were determined for #1−7, 11−18, 20−23, and 31−33. FTIR spectra were obtained for #1, 2, 4−6, 8−11, 13−15, 17−20, and 22−33. The TiO_2 was excluded from the calculation of crystal-chemical formulae. Samples 24−27 were not analyzed for the Fe oxidation state and the formulae were calculated by assuming that all Fe was Fe(III). Cation compositions for the mica component are given for samples with >5% expandable layers. The "n.d." = not determined.

https://doi.org/10.1346/CCMN.2017.064061 Published online by Cambridge University Press

were analyzed using conventional wet chemical analysis and sample 103 was analyzed by microprobe analysis using a CamScan MV-2300 electron microscope supplied with an energy-dispersion appliance INCA-200 (Oxford Instruments, Oxfordshire, UK). Elemental oxide concentration for sample 821-057 was commercially obtained by XRAL Laboratories, Toronto, Canada, and determined using X-ray fluorescence spectrometry (Table 3).

Samples TAIH, 69, Z1, E8/2, and BP are smectite-free, but the other samples contain small amounts of smectite interlayers (1−14%, Table 1). For samples 560/3, 555A, 60, 553/1, 400/3, 402/1, 37/71, 37/71A, 103, 551, 556, 575, and 2076A, the contents of smectite interlayers were determined using a new technique developed by Sakharov and Drits (2018). For samples 68-69, BAB, and PILT, the expandable layer contents were determined by Drits *et al.* (2010) and the expandable layer contents of other samples were taken from the respective publications in Table 1.

The structural formulae were calculated for a half unit cell (p.h.f.u., $O_{10}(OH)_2$). For samples that contained ⩾5% expandable layers, the corresponding molar contribution of the smectite layers to the average structural formula was subtracted to provide the structural formulae for the mica-like components (Table 2). The dehydrated smectite layers were assumed to have a negative charge equal to 0.60 valence units (*vu*) because of the specific location at the interface between mica fundamental particles (Drits *et al.*, 2010). The particular cation composition depends on the octahedral Fe content. For samples with Fe(III) ⩽ 0.5 cations p.h.f.u., the smectite component was subtracted according to the procedure described by Drits *et al.* (2010). In cases with Fe(III) > 0.5 cations p.h.f.u., the smectite formula was assumed to be $M_x(Si_{4-y}Al_y)(R(III)_{2-x+y}Mg_{x-y})O_{10}(OH)_2$, where M = (½Ca, Na), x = 0.6, and y is the same as in the average formula, R(III) = (Fe(III), Al). The amount of octahedral Al cations is assumed the same as in the average formula so that the number of Fe(III) cations p.h.f.u. is $2 - x + y - {}^{VI}Al$.

XRD and determination of unit-cell parameters

The XRD data and unit-cell parameters for samples 60/3, 68-69, PILT, BAB, TAIH, 69, and Z1 were obtained by Drits *et al.* (2010), the data for samples BP and E8/2 from Muller *et al.* (2000), and the data for samples 60, 402/1, 551, and 400/3 from Drits *et al.* (2013) (Table 4). The unit-cell parameters obtained for celadonite 69 from synchrotron data (Drits *et al.*, 2010) coincide with those reported in an electron-diffraction structure refinement of the same sample (Zhukhlistov, 2005).

Random powder XRD patterns for samples 560/3, 555A, and 103 (Figures 1a, 1b, 1c), as well as samples 37/71A, 553/1, 2076A, and KUL2, were collected using a Bruker D8 diffractometer (Bruker AXS, Karlsruhe, Germany) (40 kV, 40 mA, Bragg-Brentano θ-θ mode with a 250 mm goniometer radius). Scans were acquired from 16.0 to 64.0º2θ using a 0.05º2θ step increment and a count time of 180 s per step using Cu $Ka_{1,2}$ radiation and a Ni filter. The divergence, antiscatter, and detector slits were 0.5º, 0.5º, and 0.1º. Analysis of the experimental powder XRD patterns showed that the samples were monomineralic dioctahedral 1*M* mica varieties.

The unit-cell parameters for samples 103, 37/71A, 560/3, 555A, 553/1, 2076, and KUL2 (Table 4) were evaluated by the trial and error method based on the equations that relate $d(001)$, $d(060)$, $d(11\bar{2})$, $d(112)$, $d(22\bar{1})$, and $d(\bar{1}31)$ to a, b, c, and β (Sakharov *et al.*, 1990; Drits *et al.*, 1993b). For these samples, as well as for samples 60, 553/1, 400/3, 402/1, 37/71, 551, 556, and 575, the values of $d(001)$ were determined by Sakharov and Drits (2018). The unit-cell parameters for samples 60, 551, 402/1, and 400/3 (Drits *et al.*, 2013) were re-evaluated accordingly and the b values for samples 556 and 575 were taken from Drits *et al.* (2013) (Table 4).

FTIR spectroscopy

The infrared absorption spectra of samples 60/3, BSh11, KUL1, 68/69, PILT , 821-057, K294, GT 7-66, GT 8-69, 79/73, 372/70, TAIH, 69, and Z1 were recorded using a Nicolet ESP-260 FTIR spectrometer (Thermo Fisher Scientific, Waltham, Massachusetts, USA) in the mid-IR (MIR) region (400-4000 cm^{-1}) using the sample-preparation technique, experimental procedure, and spectra manipulations described by Zviagina *et al.* (2004). The decomposed and curve-fitted OH-stretching regions of samples BSh11 and KUL1 were published previously (Dainyak *et al.*, 2009).

Table 3. Chemical composition of samples 37/71, 103, 37/71A, and 821−057, wt %.

Sample No.	Oxides										
	SiO_2	Al_2O_3	Fe_2O_3	FeO	MgO	CaO	Na_2O	K_2O	H_2O^+	H_2O^-	Σ
37/71	49.37	9.51	21.08	1.61	4.14	0.07	0.11	7.84	5.52	1.00	100.25
103	49.90	8.02	20.75	1.81	3.65	absent	absent	7.90	–	–	92.03
37/71A	47.49	12.27	17.08	3.11	2.49	absent	0.09	7.12	8.21	1.66	99.53
821−057	50.4	6.69	22.1	n.d.	3.75	0.4	0.01	7.2	–	–	90.59

Note: The ratio Fe(III)/Fe(II) in sample 103 was assumed to be similar to that of sample 3771 based on a similar geological setting and overall cation composition.

https://doi.org/10.1346/CCMN.2017.064061 Published online by Cambridge University Press

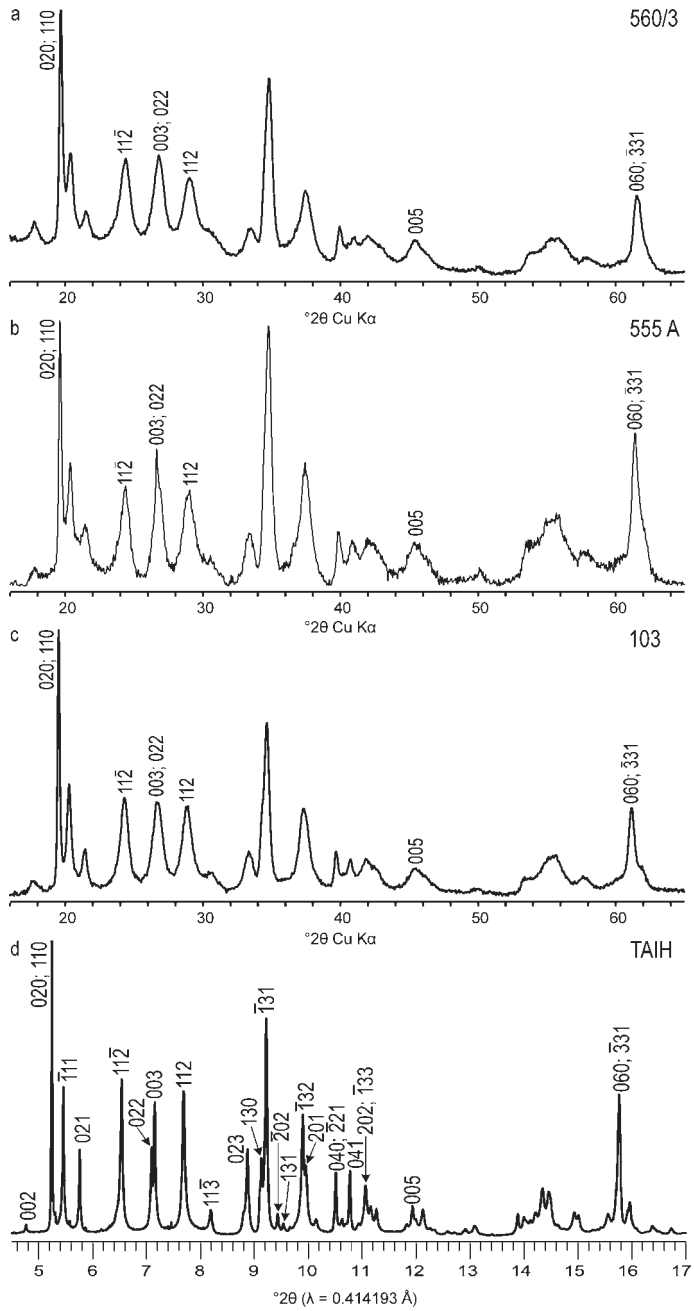

Figure 1. Powder XRD patterns of (a) Fe-illite 560/3, (b) Al-glauconite 555A, (c) glauconite 103, and (d) celadonite TAIH. The XRD pattern of sample TAIH recorded by synchrotron radiation was taken from Drits *et al*. (2010).

For samples 60, 560/3, 553/1, 2076, BSh12, KUL2, 400/3, 402/1, 551, 555A, 103, 37/71, 37/71A, and 541, the IR spectra were obtained using a Bruker VERTEX 80v FTIR spectrometer (Bruker Optics, Ettlingen, Germany) equipped with a DTGS KBr detector and KBr beam splitter. For each sample, 256 scans were recorded under vacuum in the MIR region (400-4000 cm^{-1}) with a resolution of 4 cm^{-1}. To obtain a KBr pellet, a 0.5 mg of sample was dispersed in 200 mg of KBr and the resulting mixture was placed in a 13 mm pellet die and pressed under vacuum for 10−15 min. The KBr pellet was placed into a glass desiccant box with $CaCl_2$ and heated in a furnace at 105ºC for at least 20 h.

Spectra manipulations were performed using the OPUS 7.0 software package (Bruker Ltd., Billerica, Massachusetts, USA). Baseline correction was made automatically using the concave rubber band method with 64 baseline points and 10 iterations.

https://doi.org/10.1346/CCMN.2017.064061 Published online by Cambridge University Press

Table 4. Unit-cell parameters of Fe-bearing micas 1*M* (sample numbers as in Tables 1 and 2).

	Illites and Fe-illites							Al-glauconites				
#	1	2	3	4	5	6	7	11	12	13	14	15
Sample	60	60/3	BP	560/3	553/1	2076A	575	400/3	556	KUL2	551	555A
a (Å)	5.22	5.235	5.219	5.238	5.227	5.244	n.d.	5.236	n.d.	5.263	5.231	5.238
b (Å)	9.042	9.032	9.03	9.042	9.048	9.042	9.036	9.069	9.066	9.054	9.06	9.054
c (Å)	10.131	10.14	10.153	10.153	10.171	10.156	n.d.	10.166	n.d.	10.16	10.174	10.168
β (º)	101.3	101.5	101.4	101.3	101.3	101.2	n.d.	101.1	n.d.	101.2	100.9	101.2
*c*sinβ(Å)	9.935	9.936	9.954	9.956	9.974	9.963	9.966	9.975	9.985	9.966	9.990	9.974
*c*cosβ/*a*	-0.380	-0.387	-0.383	-0.380	-0.381	-0.376	n.d.	-0.375	n.d.	-0.376	-0.368	-0.377

	Glauconites								Celadonites		
#	16	17	18	19	20	21	22	23	31	32	33
Sample	E8/2	402/1	103	37/71	37/71A	BAB	PILT	68-69	TAIH	69	Z1
a (Å)	5.23	5.237	5.253	n.d.	5.271	5.248	5.246	5.246	5.231	5.227	5.229
b (Å)	9.066	9.07	9.084	n.d.	9.085	9.074	9.066	9.076	9.051	9.052	9.051
c (Å)	10.183	10.170	10.172	n.d.	10.181	10.203	10.182	10.184	10.138	10.153	10.144
β (º)	101.3	101.0	100.86	n.d.	100.9	101.4	101.2	101.1	100.7	100.5	100.6
*c*sinβ(Å)	9.984	9.984	9.990	9.986	9.998	10.002	9.988	9.994	9.961	9.982	9.971
*c*cosβ/*a*	-0.383	-0.370	-0.365	n.d.	-0.365	-0.384	-0.377	-0.374	-0.360	-0.355	-0.356

RESULTS

Crystal-chemical data

According to the crystal-chemical formulae, the mica structures showed a wide variety of cation compositions and can be divided for the purpose of this analysis into four groups based on the values of $K_{Al} = {}^{VI}Al/({}^{VI}Al + {}^{VI}Fe(III))$ and $Al_{total} = {}^{IV}Al + {}^{VI}Al$. The first group includes samples with $K_{Al} \geqslant 0.65$ and $Al_{total} = 1.15$ to 1.7 cations p.h.f.u. (samples 1 to 10 in Tables 1 and 2). According to the conventional nomenclature, these samples should be termed illites. This group in turn was subdivided into two subgroups. The first subgroup included samples 60 and 60/3 with $K_{Al} \sim 0.9$ and $Al_{total} \sim 1.7$ cations p.h.f.u. and relatively low contents of Fe cations ($Fe_{total} = Fe(III) + Fe(II) = 0.29$ and 0.28 cations p.h.f.u., respectively); the second subgroup included the rest of the samples in the illite group (samples 3 to 10, Tables 1 and 2) with $K_{Al} = 0.65$ to 0.75, $Al_{total} = 1.15$ to 1.65, and $Fe_{total} = 0.54$ to 0.74 cations p.h.f.u.. These samples will be hereinafter referred to as Fe-illites, whereas samples 60 and 60/3 should be treated as Mg-rich illites (Zviagina *et al*., 2015). The second group (samples 11 to 15, Tables 1 and 2) included Al-glauconites, *i.e*. samples with compositions intermediate between illites and glauconites with $K_{Al} = 0.51$ to 0.61, $Al_{total} = 1.14$ to 1.28, and $Fe_{total} = 0.79$ to 0.93 cations p.h.f.u.. The third group included glauconites proper (samples 16 to 30, Tables 1 and 2) with $K_{Al} = 0.22$ to 0.49, $Al_{total} = 0.70$ to 1.15, and $Fe_{total} = 0.89$ to 1.26 cations p.h.f.u.. The tetrahedral cation composition in these three groups of samples varies in a relatively narrow range ($0.3 \leqslant {}^{IV}Al \leqslant 0.5$ in all the samples except glauconite 402/1, where ${}^{IV}Al = 0.2$ cations p.h.f.u.). The fourth group included celadonites (samples 31 to 33, Tables 1 and 2) and is characterized by extremely low Al contents with $K_{Al} = 0.05$ to 0.13, $Al_{total} = 0.09$ to 0.44, ${}^{IV}Al = 0.05$ to 0.16 cations p.h.f.u., and very high Fe contents ($Fe_{total} = 1.17$ to 1.51 cations p.h.f.u.).

XRD data

All the samples under study have *trans*-vacant (*tv*) 1*M* structures and the powder XRD patterns show reflection positions and intensity distributions typical for *tv* 1*M* micas: the 02*l* and 11*l* region contains the most intense 020 peak and strong reflections at $11\bar{1}$, $11\bar{2}$, and 112 and a much weaker $11\bar{3}$ peak (Zviagina *et al*., 2007). Closer inspection, however, revealed differences in the reflection positions, and the most important differences were significantly lower *d*(003) and *d*(005) values in celadonites. The 003 and 022 reflections are, therefore, resolved in the celadonite XRD patterns and overlap in the Fe-illite, Al-glauconite, and glauconite XRD patterns (Figure 1). These differences in the positions of 003 and 005 reflections are also evident in the XRD patterns obtained from oriented specimens with <5% expandable layers. More reliable conclusions, however, should be made based on the random powder XRD data.

Unit-cell parameters. Samples 60 and 60/3 showed unit-cell parameters typical for Mg-rich illite (Zviagina *et al.*, 2015), *i.e*. the layer-to-layer distance values *c*sinβ = 9.935 and 9.936 Å, the *b* parameters of 9.042 and 9.032 Å and the layer displacement values, *c*cosβ/*a* =

https://doi.org/10.1346/CCMN.2017.064061 Published online by Cambridge University Press

−0.380 and −0.387, respectively (Table 4). The Fe-illite structures have similar lateral dimensions and layer displacement values (b = 9.030 to 9.048 Å, $c\cos\beta/a \approx -0.38$), but larger layer-to-layer distances. The layer-to-layer distance is ~9.96 Å in most of the Fe-illite samples, except for sample 553/1 with $c\sin\beta$ = 9.980 Å. The Al-glauconites have greater layer-to-layer distances and lateral dimensions, but slightly smaller absolute layer displacement values ($c\sin\beta$ = 9.966 to 9.990, b = 9.054 to 9.069, and $c\cos\beta/a$ = −0.377 to −0.368). Glauconites showed still larger layer-to-layer distances and lateral dimensions with $c\sin\beta$ values of up to 10 Å and b parameters of up to 9.085 Å and $c\cos\beta$/a = -0.364 to -0.384. In comparison to glauconites, celadonite samples have smaller layer-to-layer distances ($c\sin\beta$ = 9.961 to 9.982 Å) and reduced lateral dimensions ($b \approx$ 9.95 Å) and layer displacements ($|c\cos\beta/a|$ = 0.355 to 0.364).

FTIR spectroscopy

The absorption band positions in the sample FTIR spectra MIR region were assigned to specific vibration modes (Table 5 and Figure 2) by following the interpretations of Farmer (1974), Russell and Fraser (1994), Besson and Drits (1997a, 1997b), Madejova and Komadel (2001), and Madejova (2003). The FTIR spectra of all the samples are typical for dioctahedral micas. Depending on the specific cation composition, the 600−950 cm^{-1} region showed the following bands:

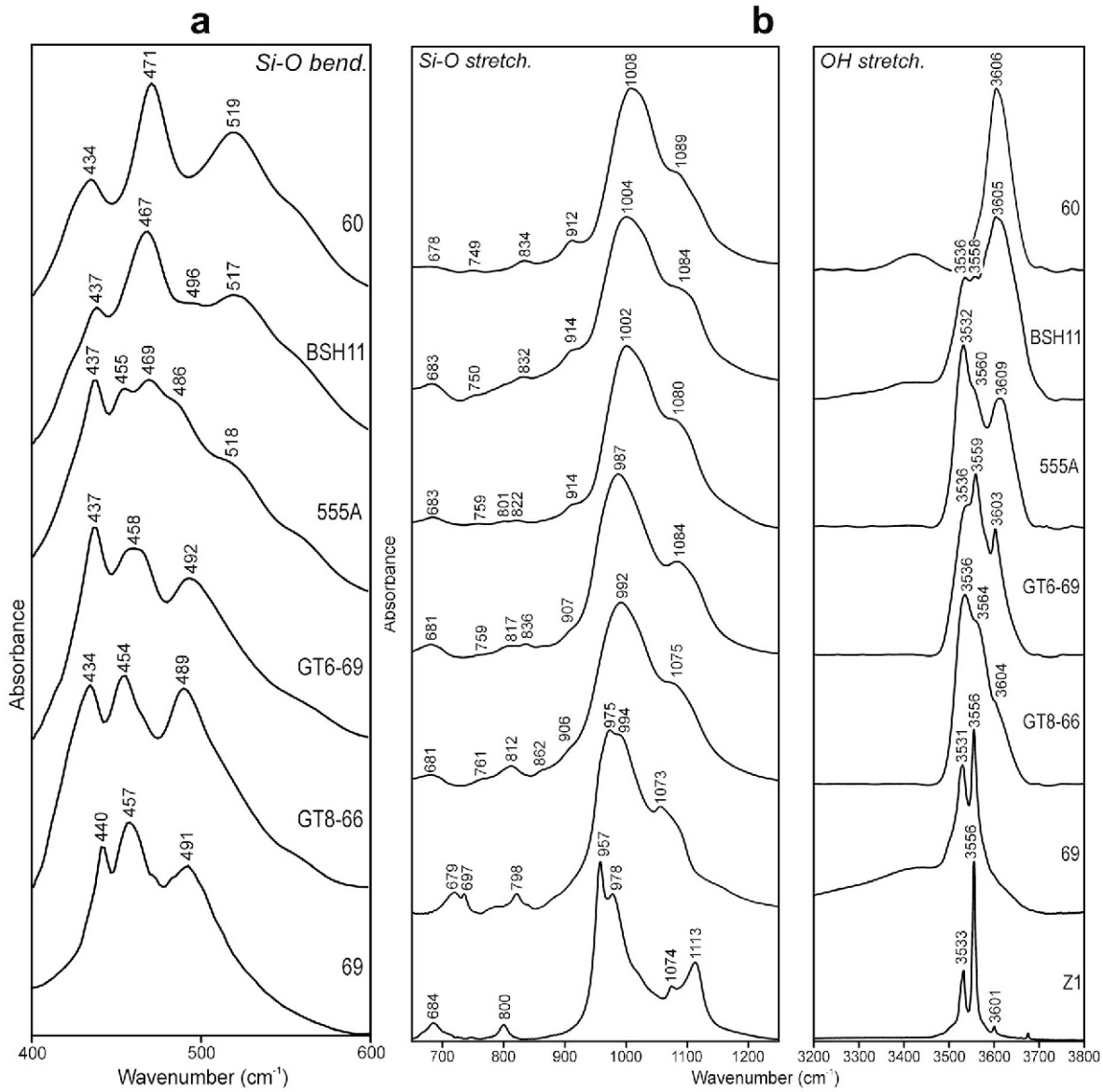

Figure 2. Selected FTIR spectra of Fe-bearing dioctahedral micas (illite 60, Fe-illite BSH11, Al-glauconite 555A, glauconites GT6-69 and GT8-66, celadonite 69, celadonite Z1) in the regions (a) 400−600 cm^{-1} and (b) 600−1300 cm^{-1} and 3200−3800 cm^{-1}.

https://doi.org/10.1346/CCMN.2017.064061 Published online by Cambridge University Press

Table 5. Selected characteristic bands in the MIR region of the FTIR spectra of Fe-bearing micas 1M (cm^{-1}) (sample numbers as in Tables 1 and 2).

#	Sample	Si-O bend	Si-O-Si bend	Si-O-Si bend (additional)	Si-O-Al bend	Si-O-Fe bend	Si-O stretch	Si-Oap stretch	OH-stretch, visually discernable absorption maxima			
1	60	434	471	–	519	–	1008	1089	–	–	–	3606
2	60/3	435	470	–	519	–	1010	1084	–	–	–	3607
4	560/3	436	471	–	518		1008	1084	3528	–	–	3612
5	553/1	434	471	451sh	526	–	1017	1083sh	3534	–	–	3624
6	2076	437	469	453	517	486sh	1000	1085	3530	3554	–	3607
8	BSh11	437	467	450sh	517	496*	1004	1084	3536	3558	–	3605
9	BSh12	437	467	–	515	–	1007	1084	3534	3555sh	3582sh	3602
10	KUL1	438	467	454sh	514	490	998	1087	3533	3554	3584	3602
11	400/3	438	468	455sh	515sh	484sh	994	1079	3532	3555sh	–	3603
13	KUL2	438	469	454sh	518	484sh	1012	1081sh	3533	3555sh	–	3602, 3618sh
14	551	434	465	454	514sh	486sh	1006	1084sh	3533	3560sh	–	3610
15	555A	437	469	455	518sh	486sh	1002	1080sh	3532	3560sh	–	3609
17	402/1	438	453	467	–	483sh	990	1082	3533	3555sh	–	3603*
18	103	434	455	–	–	491	991	1074	3537	3559	–	3602sh
19	37/71	434	456	–	–	491	995	1072	3535	3561	–	3603sh
20	37/71A	435	457	–	–	487	1001	1079sh	3538	–	3581sh	3603sh
22	PILT	439	459	–	–	494	1010	1081sh	–	3550	–	
23	68/69	437	457	–	–	494	1013	1082sh	3550 (3530+3542+3567)**		–	
24	G294	435	463	–	–	499sh	995	1082	3534	3558		3604
25	GT6-69	437	458	–	–	492	987	1084	3536	3559	3583sh	3603
26	GT8-66	434	454	–	–	489	992	1075	3536	3564sh		3604sh
27	821-057	438	456	–	–	492	992	1078	3538	3568		3602
28	541	438	458	–	526sh	483	1000	1072	3533	3558	–	3621
29	79/73	439	461	–	–	496	1016	1099sh	3553 (3537+3558)**		–	3601sh
30	372/70	440	460	–	–	496	1014	1101	3550 (3538+3563)**		–	3614sh
31	TAIH	439	459	–	–	493	978	1090	3532	3556	–	3601
32	69	440	457	–	–	491	975, 995sh	1072, 1100sh	3533	3555sh	–	3603**
33	Z1	n.d.	n.d.	–	–	n.d.	957, 978	1074, 1113	3533	3556	–	3601

* Weak, ** Determined from the second derivative, sh = shoulder, n.d. = not determined.

an AlOHAl bending mode (910–915 cm^{-1}); AlOHFe(III) and Fe(III)OHFe(II) bending vibrations at 870 and 820 cm^{-1}, respectively; the AlOHMg bending mode at 835–840 cm^{-1} coupled with an Al-O out-of-plane vibration at 820–830 cm^{-1}; the Si-O bands (695–700 cm^{-1}); the Al-O-Si in-plane (750–755 cm^{-1}), and coupled Al-O and Si-O out-of-plane vibrations (~620 cm^{-1}, in samples with Al-for-Si substitution) were at ~620 cm^{-1}.

The distinguishing features for all groups of mica varieties mostly involve the most intense absorption band from the Si-O stretching mode at ~1000 cm^{-1}, three characteristic sharp bands in the Si-O bending region (400–550 cm^{-1}), and the OH-stretching region band positions and profile with a maximum intensity at ~3600–3630 cm^{-1} (Figure 2 and Table 5). According to the FTIR characteristics, the studied samples fell into several groups depending on the K_{Al} = Al/(Al + Fe(III)) value.

K_{Al} = 0.91 ((Mg, Fe)-rich illites, samples 60 and 60/3; #1 and 2 in Tables 1, 2, and 5). The OH stretching region shows a broad band, which is a superposition of individual cation-OH-cation vibrations with maximum values at 3606 and 3607 cm^{-1} that correspond to the AlOHMg vibration. The Si-O bending region shows three bands at 434–435, 470–471, and 519 cm^{-1}, which were termed δ_1, δ_2, and δ_3, respectively, with δ_2 the strongest mode (Figure 2a, sample 60). The Si-O stretching region is an intensive band at 1008–1010 cm^{-1} with a distinct shoulder at 1084–1089 cm^{-1} corresponding to the Si-O apical stretching vibration.

K_{Al} = 0.61 to 0.75 (Fe-illites; Al-glauconites with Fe_{total} ~0.8 cations p.h.f.u.: #4 to 6, #8 to 11, and #13, Tables 1, 2, and 5). The OH stretching region contains two well resolved bands at 3528–3536 and 3602–3624 cm^{-1}. The 3528–3536 cm^{-1} band is a superposition of individual vibrations that involve Fe(II), Fe(III), and Mg(Fe(II)OHFe(III), Fe(III)OHFe(III), and Fe(III)OHMg, etc., see Discussion) with a maximum that corresponds in most cases to the Fe(III)OHFe(III) band. The 3605–3624 cm^{-1} bands are from vibrations that involve Al and Mg with a maximum that corresponds to AlOHMg (most samples), AlOHAl (553/1), or the superposition of AlOHMg and AlOHAl. In several cases, the two bands have distinct shoulders that correspond to the Fe(III)OHMg and (samples BSh12, KUL1) MgOHMg vibrations (Table 5). The "Al, Mg" band is either stronger than or of similar intensity as the "Fe" band.

The Si-O bending region shows three bands at 434–438, 467–471 (the strongest), and 514–526 cm^{-1} (similar to (Mg, Fe)-rich illites 60 and 60/3). At the same time, most samples in this group (except 560/3 and BSH12) also have minor bands or shoulders at positions typical for the δ_2 and δ_3 Si-O bending bands of glauconites and celadonites (see below) at 450–455 and 484–496 cm^{-1}. The Si-O stretching vibration is located at 994–1017 cm^{-1} with the Si-O apical stretching mode either as a shoulder or as a resolved band at 1079–1087 cm^{-1}.

K_{Al} ~ 0.5 (Al-glauconite samples with Fe_{total} ~ 0.9 cations p.h.f.u.: 551 and 555A; #14 and 15 in Tables 1, 2, and 5). The OH stretching region is similar to the previous group (two bands at 3532–3533 and 3609–3610 cm^{-1}), but the "Fe" band has a Fe(III)OHMg shoulder that is stronger than the "Al, Mg" band. In the Si-O bending region, samples 551 and 555A have three bands of similar intensity: a sharp, well resolved δ_1 mode at 434 and 437 cm^{-1} and two distinct bands at 465–469 and 454–455 cm^{-1}. In addition, the bands display shoulders at 514–518 and 486 cm^{-1}. The Si-O stretching region is similar to the previous groups and shows a strong band at 1002–1006 and a shoulder at 1080–1084 cm^{-1} (the Si-O apical vibration).

K_{Al} = 0.21 to 0.49 (glauconites: #17 to 20 and #22 to 30 in Tables 1, 2, and 5). The glauconite spectra display a wide variety of profiles and intensity distributions in the OH stretching region. The typical feature for most of the spectra is the presence of maxima at 3530–3538 cm^{-1} and ~3550–3560 cm^{-1} that correspond to Fe(III)OHFe(III) and Fe(III)OHMg, respectively. The maxima can be either well resolved or poorly resolved, can range from sharp bands to shoulders, and can have similar or different intensities. In addition, most of the spectra show much weaker bands or shoulders at 3600–3605 cm^{-1}, which are attributed to the AlOHMg vibration. The Si-O bending region has three characteristic bands, δ_1, δ_2, and δ_3, at 434–440, 454–467, and 483–499 cm^{-1}, respectively. Either the δ_1 or δ_2 can be the strongest or can have similar intensities. The Si-O stretching region in glauconite spectra show a diversity of profiles that range from single asymmetric bands with a hardly discernable shoulder to two well resolved bands with the Si-O stretching mode at 990–1016 cm^{-1} and the Si-O apical vibration at 1072–1101 cm^{-1}.

K_{Al} = 0.05–0.13 (celadonites: samples Z1, 69, and TAIH; #31 to 33 in Tables 1, 2, and 5). The FTIR characteristics obtained for samples Z1, TAIH, and 69 are in good agreement with those reported previously (Buckley *et al*., 1978; Slomimskaya *et al*., 1986; Besson and Drits, 1997a; Weiszburg *et al*., 2004). The O-H stretching region contains two sharp bands with a stronger band at ~3556 cm^{-1} (Fe(III)OHMg) and a less intense band at 3532–3533 cm^{-1} (Fe(III)OHFe(III)). In addition, these spectra may show minor sharp maxima at ~3600 cm^{-1} (AlOHMg) (samples TAIH and Z1) and shoulders at ~3500 cm^{-1} (samples TAIH and 69), which may be attributed to the Fe(II)OHFe(II) vibration. The

https://doi.org/10.1346/CCMN.2017.064061 Published online by Cambridge University Press

three characteristic bands in the Si-O bending region, δ_1, δ_2, and δ_3, are at 439–440, 457–459, and 491–493 cm^{-1}. In the Si-O stretching region, the celadonite spectra show sharp, well resolved bands with either two bands at 975–978 and 1072–1090 cm^{-1} with or without shoulders (see Table 5) or four bands at 957, 978, 1074, and 1113 cm^{-1} (sample Z1, Figure 2b).

DISCUSSION

Unit-cell parameters and cation composition

Layer-to-layer distance. The dependence of *c*sinβ values on cation composition in Fe-bearing, K-dioctahedral micas is controlled by two competing factors. On the one hand, the layer-to-layer distance tends to decrease with a decrease in Al for Si substitution. This is a trend previously reported for the illite-aluminoceladonite series, where *c*sinβ values decrease monotonously from ~10 Å in (Mg, Fe)-poor illites to 9.94–9.96 Å in Mg-rich illites to ~9.92 Å in aluminoceladonites (Drits *et al*., 2010; Zviagina *et al*., 2015). This is associated with a decrease in the interlayer distance that results from the weakening of the mutual repulsion of tetrahedral anion basal surfaces across the interlayer with a decrease in negative charge compensation of the basal oxygens. In all the Fe-bearing micas under study except celadonites, the tetrahedral cation composition varies within a relatively narrow range. The influence of this factor, therefore, only becomes significant in celadonites which contain very little or no tetrahedral Al and have reduced *c*sinβ values (9.96–9.98 Å) in comparison to glauconites with *c*sinβ values up to 10 Å. On the other hand, as the larger Mg, Fe(III) and Fe(II) octahedral cation contents are increased, the octahedral size and the octahedral sheet thickness increase and lead to an increase in 2:1 layer thickness (Drits *et al*., 2010; Zviagina and Drits, 2012). The layer-to-layer distance, therefore, increases from Mg-rich illite (~9.94 Å) to Fe-illite (~9.96 Å) to Al-glauconite and glauconite (up to 10 Å) because variations in the tetrahedral cation composition and, therefore, in interlayer distances are not significant (Figure 3). On the whole, the dependence of *c*sinβ values on octahedral cation composition in Fe-bearing dioctahedral micas can be described, with an *esd* = 0.007 Å and R^2 = 0.90 (Figure 4), by the regression equation:

$$c\sin\beta = 10.004 - 0.046(^{IV}Al - 0.545)^2 - 0.111(Mg - 0.302)^2 - 0.538(Fe(II) - 0.256)^2 - 0.051(Fe(III) - 1.242)^2 \quad (1)$$

where ^{IV}Al, *Mg*, *Fe(II)* , and *Fe(III)* are the numbers of cations p.h.f.u.

Layer displacement. As the content of the larger octahedral Mg, Fe(II), and Fe(III) cations increases, the absolute value of the layer displacement *c*cosβ/a decreases, so that

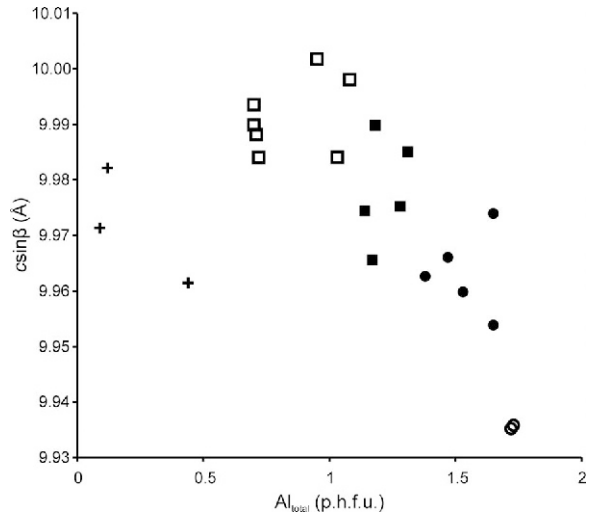

Figure 3. The observed *c*sinβ values plotted *vs.* Al_{total} contents (cations p.h.f.u.). Symbols: open circles = Fe-bearing, Mg-rich illites; black circles = Fe-illites; black squares = Al-glauconites; open squares = glauconites; and crosses = celadonites.

$$c\cos\beta/a = -0.384 + 0.256(Mg - 0.447)^2 + 0.009(Fe(III) - 0.397)^2 + 0.467(Fe(II) - 0.151)^2 \quad (2)$$

(esd = 0.004, R^2 = 0.91, Figure 5, variables defined as in equation 1). As the size difference between the occupied and the vacant octahedra decreases with increased contents of larger Mg and Fe cations, the *c*cosβ/a values become closer to the idealized value of –1/3 (Drits *et al*., 2006; Zviagina *et al*., 2015).

The b parameter. The dependence of *b* on the cation composition in Fe-bearing, K-dioctahedral micas 1*M* is controlled by the same factors as in the illite-aluminoceladonite series described by Zviagina *et al.* (2015). The actual mica-structure lateral dimensions can be seen

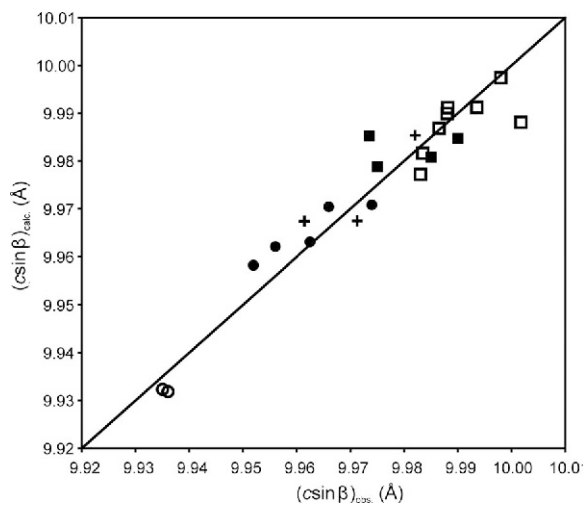

Figure 4. Calculated (equation 1) *c*sinβ parameters plotted *vs.* observed values. Symbols are the same as in Figure 3.

https://doi.org/10.1346/CCMN.2017.064061 Published online by Cambridge University Press

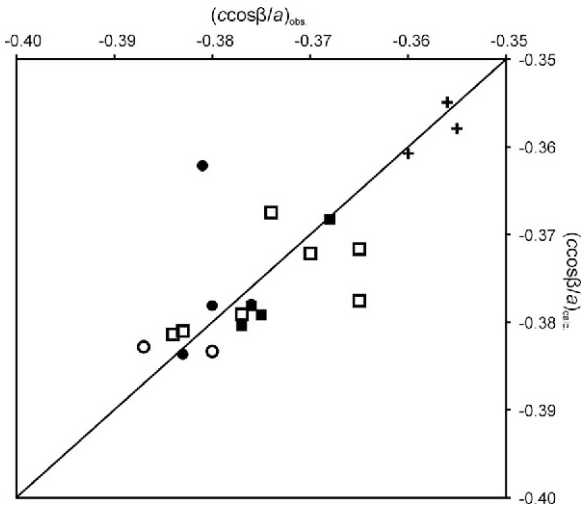

Figure 5. Calculated (equation 2) *c*cosβ/a parameters plotted *vs.* observed values. Symbols are the same as in Figure 3.

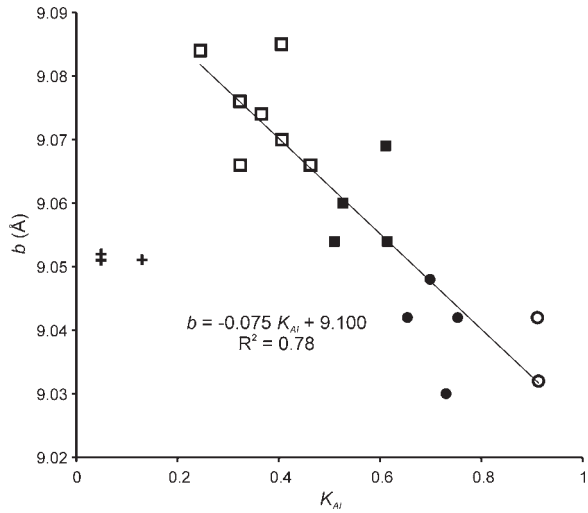

Figure 6. The observed *b* values plotted *vs.* K_{Al}. Symbols are the same as in Figure 3.

as a compromise between the larger dimensions of the idealized and unrotated tetrahedral sheet (b_t) and the smaller octahedral sheet dimensions (b_{oct}), which are related to the tetrahedral basal and the octahedral unshared lateral edge lengths. In the Mg-rich illite – Fe-illite – Al-glauconite – glauconite series, the tetrahedral Al contents vary within a relatively narrow range and *b* increases due to an increase in octahedral lateral edge lengths that result from an increase in the content of larger Mg and Fe cations. From glauconite to celadonite, however, a dramatic decrease in ^{IV}Al leads to a decrease in *b* from up to 9.085 Å in glauconites down to ~9.05 Å in celadonite. This is due to decreased tetrahedral basal edge lengths that result from the decreased size of the tetrahedra (Figure 6). Moreover, the need to adjust the increased lateral dimensions of the octahedral sheet to the reduced dimensions of the tetrahedral sheet leads to additional thickening of the octahedral sheet and, consequently, an additional decrease in the octahedral lateral dimensions and in *b*. The *b* values for all celadonites are, therefore, ~9.05 Å (see also Buckley *et al*., 1978). For all other K-dioctahedral Fe-bearing micas, however, the increase in *b* values from illites to glauconites through Fe-illites and Al-glauconites can be described by a linear trend (Figure 6). At the same time, the complicated relationship between *b* and octahedral cation composition can be described with an estimated standard deviation (*esd*) value of 0.010 Å and R^2 = 0.89 (Figure 7) by a unique regression equation for all the varieties of K-dioctahedral 1*M* micas that not only include the Fe-bearing micas under study, but also (Mg, Fe)-poor illites, Mg-rich illites, and aluminoceladonites (variables defined in equation 1, the crystal-chemical formulae for the latter three groups of samples are given in Zviagina *et al.*, 2015):

$$b = 9.098 - 0.218(Mg - 0.400)^2 - 0.015(Fe(III) - 2.207)^2 - 0.470(Fe(II) - 0.209)^2 \quad (3)$$

Each of the four groups of Fe-bearing, K-dioctahedral micas can be characterized, therefore, by a unique combination of unit-cell parameter ranges (Table 6). The illite group contains two distinct subgroups, illites proper (Fe-bearing, Mg-rich illites 60 and 60/3) and Fe-illites. Note that unlike Fe-illites, the *c*sinβ and *c*cosβ/*a* values of samples 60 and 60/3 can be described both by equations (1) and (2) and by equations obtained

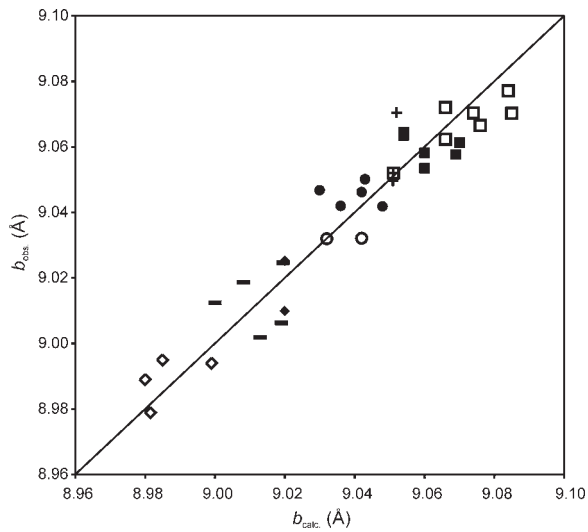

Figure 7. Calculated (equation 3) *b* parameters plotted *vs.* observed values. Symbols: Open circles = Fe-bearing, Mg-rich illites; black circles = Fe-illites; black squares = Al-glauconites; open squares = glauconites; crosses = celadonites; open diamonds = (Mg, Fe)-poor illites, black diamonds = Mg-rich illites; and bars = aluminoceladonites. The b_{obs} values for (Mg, Fe)-poor illites, Mg-rich illites, and aluminoceladonites are from Zviagina *et al.* (2015).

https://doi.org/10.1346/CCMN.2017.064061 Published online by Cambridge University Press

Table 6. Composition ranges and identification criteria for Fe-bearing, K-dioctahedral micas.

				$c\sin\beta$ (Å)	b (Å)	$\lvert c\cos\beta/a\rvert$
Fe-bearing, Mg-rich illites	K_{Al} ~ 0.9	Al_{total} ~ 1.7	Fe_{total} ~ 0.3	$c\sin\beta$ ~9.94	9.03 ⩽ b ⩽9.04	0.38–0.39
Fe illites	0.65 ⩽ K_{Al} ⩽ 0.75	1.15 ⩽ Al_{total} ⩽ 1.65	0.5 ⩽ Fe_{total} ⩽ 0.7	9.96 ⩽ $c\sin\beta$ ⩽9.98	9.03 ⩽ b <9.05	~0.38
Al-glauconites	0.5 ⩽ K_{Al} ⩽ 0.6	1.1 < Al_{total} ⩽ 1.3	0.8 ⩽ Fe_{total} < 0.9	9.97 ⩽ $c\sin\beta$ ⩽9.99	9.05 ⩽ b ⩽9.07	0.37–0.38
glauconites	K_{Al} < 0.5	0.7 ⩽ Al_{total} ⩽ 1.15	0.9 ⩽ Fe_{total} ⩽ 1.3	9.98 ⩽ $c\sin\beta$ ⩽10.0	9.07 ⩽ b ⩽9.085	0.36–0.38
Celadonites	K_{Al} < 0.2	Al_{total} < 0.45	Fe_{total} > 1.15	9.96 ⩽ $c\sin\beta$ ⩽9.98	b ~9.05	0.355–0.36
(includes Buckley samples)	(K_{Al} ⩽ 0.5)	(Al_{total} ⩽ 0.6)	(0.8 ⩽ Fe_{total} ⩽1.5)			

for the Al-rich micas in the illite-aluminoceladonite series (Zviagina *et al.*, 2015). Fe-bearing, Mg-rich illites and Fe-illites form a separate field from Al-glauconites and glauconites in the plot of $c\sin\beta$ *vs.* Al_{total} (Figure 3) as well as in the b *vs.* K_{Al} plot (Figure 6). The boundary between Fe-illites and Al-glauconites corresponds to K_{Al} values between 0.60 and 0.65 and occurs at b values of ~9.05 Å. At the same time, the variation ranges in cation compositions and unit-cell parameters in Al-glauconites and glauconites overlap (Table 6) and differentiating between them based solely on chemical and XRD data may be difficult. The distinctive features of celadonite are the relatively low values of $c\sin\beta$ and the reduced $|c\cos\beta/a|$ values in combination with b parameters that are lower than those for glauconites, but are similar to those for Fe-illites.

The results obtained in the present study appear to imply a compositional gap between glauconite and celadonite as far as the K_{Al} and Al_{total} = ^{IV}Al + ^{VI}Al values are concerned. For glauconites, 0.3 ⩽ K_{Al} < 0.5 and 0.7 < Al_{total} < 1.1 cations p.h.f.u, whereas for celadonites the values are K_{Al} < 0.2 and Al_{total} < 0.45 cations p.h.f.u. The celadonite samples described by Weiszburg *et al.* (2004) showed similar cation composition variation ranges. The celadonite samples studied by Buckley *et al.* (1978), however, displayed a wider variety of cation compositions with K_{Al} ⩽ 0.5 and Al_{total} ⩽ 0.6 cations p.h.f.u. In most glauconite samples, Si ⩽ 3.7 cations p.h.f.u, whereas in most celadonites Si ⩾ 3.8 cations p.h.f.u. The glauconite sample 402/1 and celadonite sample TAIH are exceptions with Si = 3.72 and 3.80 cations p.h.f.u, respectively. From a formal point of view and based solely on the octahedral and tetrahedral cation composition, therefore, an almost continuous compositional series may seem to exist between glauconite and celadonite (Table 6). At the same time, the celadonites, which belong to true micas, have higher interlayer occupancies than glauconites (interlayer-deficient mica varieties). This and still more importantly the dramatically different XRD and FTIR characteristics, however, confirm the conclusion of Buckley *et al.* (1978) that glauconite and celadonite should be treated as separate mineral species.

FTIR spectroscopy data

Si-O vibrations. According to Farmer (1974), the Si-O stretching vibrations are only weakly coupled with other vibrations of the structure, whereas the Si-O bending vibrations are strongly coupled with vibrations of the octahedral cations and with translational vibrations of hydroxyl groups. Whereas strong correlations are observed between the spectroscopic characteristics of Si-O bending and stretching regions and the cation compositions of tetrahedral and octahedral sheets of Fe-poor micas (Zviagina *et al.*, 2015), such correlations in Fe-bearing varieties are mostly related to the Si-O bending region and only concern the octahedral cation

https://doi.org/10.1346/CCMN.2017.064061 Published online by Cambridge University Press

composition. Considering these correlations, the cation compositions from the bulk crystal-chemical formulae (Table 2) are used because the IR vibration modes are sensitive to the cation distribution in both mica and smectite layers.

In Fe-bearing, K-dioctahedral 1*M* micas, the Si-O stretching region is the least informative for distinguishing features, except for celadonite spectra which have sharp, well resolved bands and tend to show four vibration modes (Table 5, Figure 2b). In the Si-O bending region, the position of the lower wavenumber band, δ_1, varied within a narrow range (434–440 cm^{-1}) for all the samples and the position had a very minor trend to decrease with increased Fe contents. The position of the δ_2 mode, which corresponds to the Si-O-Si bending vibration, tended to decrease with a decrease in Al and an increase in Fe cation contents from ~470 cm^{-1} in illites and Fe-illites to 454–463 cm^{-1} in glauconites and celadonites. Simultaneously, the δ_3 mode shifted from 514–526 cm^{-1} (Si-O-Al) to 483–499 cm^{-1} (Si-O-Fe) (Table 5). The shift of the δ_3 mode to lower wavenumbers with an increase in Fe for Al substitution may be associated with an increase in the Si-O-^{VI}M angle due to an increase in the octahedral sheet thickness, which in turn reduces the vibration energy (Velde, 1978). Another reason is that an increase in the total mass of cations in the vibrating system for the cations with the same valence (Si-O-Al *vs.* Si-O-Fe(III)) decreases the wavenumber (Besson and Drits, 1997b).

The samples, therefore, fall into two distinct groups: 1) for $K_{Al} \geqslant 0.6$, δ_2 is at 469 ± 2 cm^{-1} and δ_3 is at 520 ± 6 cm^{-1}; and 2) for $K_{Al} < 0.5$, δ_2 is at 458 ± 5 cm^{-1} and δ_3 is at 491 ± 8 cm^{-1} (Figures 8, 9). Samples with a highly heterogeneous cation composition, such as Fe-illites and Al-glauconites, additionally display vibration modes that are typical for the δ_2 and δ_3 values of glauconites and celadonites that are either distinct maxima of minor intensity or shoulders. Specifically, in addition to the δ_1 mode of the Si-O bending region in samples 551 and 555A (K_{Al} ~ 0.5), the Si-O bending region contained two well resolved bands at 465–469 cm^{-1} and 454–455 cm^{-1} and shoulders at 514–518 cm^{-1} and 486 cm^{-1} (Table 5, Figure 2a (sample 555A), Figures 8 and 9). Similarly, glauconite sample 402/1 (K_{Al} = 0.40) showed a second Si-O-Si bending mode at 467 cm^{-1} in addition to a δ_2 mode at 453 cm^{-1} (Table 5). On the whole, the plots of the band positions of δ_2 and δ_3 against the Fe_{total} values in Fe-bearing, Mg-rich illites; Fe-illites; Al-glauconites; glauconites; and celadonites (Figures 8, 9) have a wider point scatter than similar plots of the Si-O bending and stretching band positions of Fe-poor dioctahedral 1*M* micas against the cation composition (Zviagina *et al.*, 2015). This may be associated with the much higher degree of crystal-chemical heterogeneity in Fe-bearing varieties and especially in glauconites and Al-glauconites (Drits *et al.*, 2013).

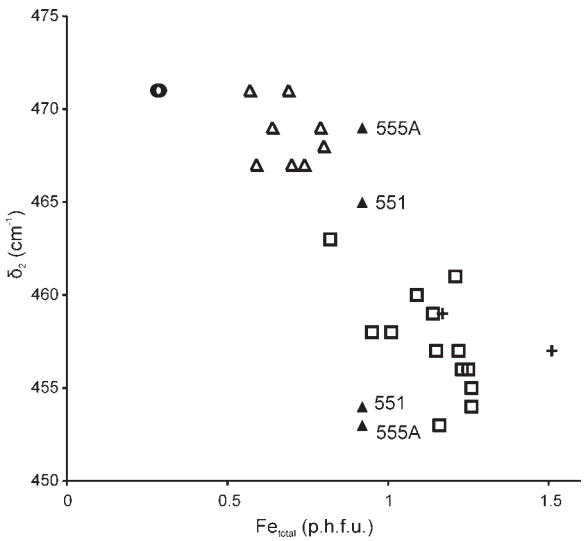

Figure 8. Band positions (cm^{-1}) of δ_2 plotted *vs.* Fe_{total} contents (cations p.h.f.u.). Symbols: open circles = Fe-bearing, Mg-rich illites (K_{Al} = 0.9); open triangles = Fe-illites and Al-glauconites (K_{Al} = 0.6–0.75); black triangles = Al-glauconites (K_{Al} = 0.5); open squares = glauconites (K_{Al} < 0.5); crosses = celadonites (K_{Al} < 0.15).

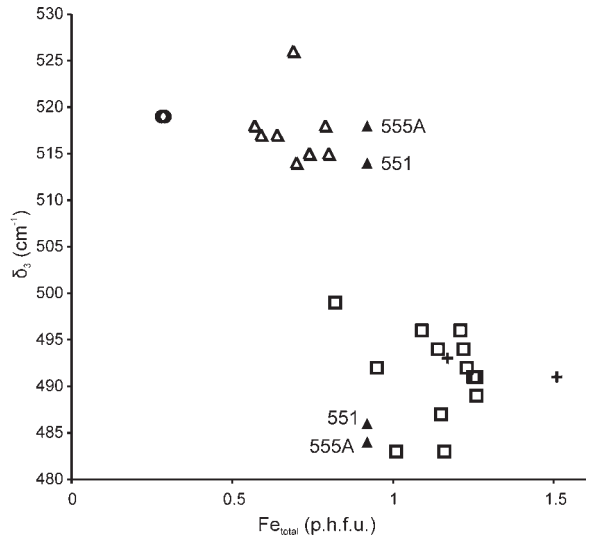

Figure 9. Band positions (cm^{-1}) of δ_3 plotted *vs.* Fe_{total} contents (cations p.h.f.u.). Symbols are the same as in Figure 8.

The OH stretching vibrations. In Fe-bearing, Mg-rich illite samples 60 and 60/3, the OH-stretching region is a wide absorption band that results from the superposition of individual cation-OH-cation vibrations, which can be identified using spectrum decomposition and curve fitting (Besson and Drits 1997a, 1997b; Zviagina *et al.*, 2015). The maximum absorption is determined by the AlOHMg vibration at 3606 and 3607 cm^{-1}, respectively (Table 5, Figure 2c). The OH-stretching regions of the

https://doi.org/10.1346/CCMN.2017.064061 Published online by Cambridge University Press

Fe-illite and Al-glauconite spectra differ dramatically from those of Fe-bearing, Mg-rich illites because the spectra contain two well resolved broad bands. One band is a superposition of individual vibrations that involve Fe and Mg with a maximum that corresponds to the Fe(III)OHFe(III) band (3532 ± 4 cm^{-1}) and the other results from vibrations that involve Al and Mg with a maximum that corresponds in most cases to AlOHMg (at 3605 ± 5 cm^{-1}). For example, the "Fe" band of Fe-illite BSH11 is a superposition of the following individual vibrations: Fe(II)OHFe(III) (3516 cm^{-1}), Fe(III)OHFe(III) (3534 cm^{-1}), AlOH Fe(II), and MgOHFe(III) (3560 cm^{-1}); whereas the "Al, Mg" band involves MgOHMg (3581 cm^{-1}), AlOHMg (3600 cm^{-1}), and AlOHAl (3619 cm^{-1}, 3637 cm^{-1}, and 3652 cm^{-1}) (Dainyak et al., 2009). In sample 560/3, the "Al, Mg" band at 3614 cm^{-1} results from a superposition of the AlOHMg and AlOHAl vibrations. In sample 553/1, the maximum absorption in this band (3624 cm^{-1}) is determined by the AlOHAl vibration. For $K_{Al} \geqslant 0.6$, the intensity of the "Al, Mg" band is either greater than or similar to the "Fe" band (*e.g.*, sample BSH11, Figure 2c), but for $K_{Al} \sim 0.5$, the "Fe" band is stronger (sample 555A, Figure 2c).

Similar to illites, Fe-illites, and Al-glauconites, the OH-stretching vibration regions of glauconites result from a superposition of individual cation-OH-cation modes but, with few exceptions, the resolution is worse than in Al-glauconites. The distinguishing feature of glauconite spectra is the presence of maxima at 3533–3538 cm^{-1} and ~3550–3560 cm^{-1} (that correspond to Fe(III)OHFe(III) and Fe(III)OHMg, respectively), which can be either well resolved or poorly resolved (from sharp bands to shoulders) and have similar or different intensities.

The OH-stretching regions of celadonites differ dramatically from those of all the other mica varieties in the series. The spectra show two sharp, well resolved maxima, the stronger at 3556 cm^{-1} (Fe(III)OHMg) and a less intense maximum at 3532–3533 cm^{-1} (Fe(III)OHFe(III)). In addition, the AlOHMg stretching mode can appear as a minor sharp band (samples TAIH and Z1). As shown by Besson *et al.* (1987), the high resolution of the OH-stretching spectral region of celadonites is associated with the high degree of ordering in the octahedral cation distribution.

The band positions and profile in the Si-O bending and OH-stretching regions, therefore, provide diagnostic information that allows a distinction between (a) illites proper, (b) Fe-illites and Al-glauconites, (c) glauconites, and (d) celadonites (Table 7).

Table 7. FTIR distinctive features for Fe-bearing, K-dioctahedral micas (see text for details and explanation).

	Si-O-Si bend (δ_2, cm^{-1})	Si-O-Al bend (δ_3, cm^{-1})	Si-O-Fe bend (δ_3, cm^{-1})	OH stretch
Fe-bearing, Mg-rich illites ($K_{Al} \sim 0.9$)	~470	~520	–	Broad band . maximum at 3600–3610 cm^{-1}
Fe illites ($0.65 \leqslant K_{Al} \leqslant 0.75$) and Al-glauconites ($0.5 < K_{Al} \leqslant 0.6$)	467-471; 450-455(* or sh)	514-526	484-496	Two bands, 3528-3534 ("Fe") and 3600-3610 cm^{-1} ("Al, Mg") Similar intensity or "Al, Mg" band stronger
Al-glauconites ($K_{Al} \sim 0.5$)	465-469; 454-455	514-518 (sh)	486 (sh)	"Fe" band stronger
Glauconites		–	483-499	Bands at 3533-3538 cm^{-1} and ~3550–3560 cm^{-1}, variable resolution and relative intensity
Celadonites	453-463			Sharp, well resolved bands at 3556 and 3532–3533 cm^{-1}

CONCLUSIONS

A detailed analysis of the chemical and XRD data of a set of Fe-bearing mica samples that ranged in composition from illite and Fe-illite to celadonite

https://doi.org/10.1346/CCMN.2017.064061 Published online by Cambridge University Press

through Al-glauconite and glauconite has shown that each group in the series is characterized by a unique combination of structural and crystal-chemical features. Composition ranges have been proposed and identification criteria have been formulated for each of the mica groups (Table 6). The results obtained suggest that the conventional mica classification be revised to characterize illites by $K_{Al} \geqslant 0.65$. In addition, a revised nomenclature should take into account the subdivision of the illite group into illites proper and Fe-illites, as well as the existence of mica samples with an Al-glauconite composition.

The dependences of the unit-cell parameters, $c\sin\beta$ and $c\cos\beta/a$, on cation composition in Fe-bearing, K-dioctahedral micas are governed by different regularities and are described by different relationships in comparison to the Al-rich micas in the series, (Mg, Fe)-poor illites, Mg-rich illites, and aluminoceladonites. Fe-bearing illites with $Fe_{total} \sim 0.3$ cations p.h.f.u. and $Al_{total} \sim 1.7$ can be described by both sets of relationships. The relationship between the *b* unit-cell parameter and the cation composition can be described by a unique regression equation for all K-dioctahedral 1*M* micas.

Mica variety identification in this series cannot be based solely on chemical analysis and should also include structural data and spectroscopic data. Specifically, the distinctive features of celadonites, apart from cation composition and unit-cell parameters, include the shapes and profiles of FTIR spectra and the sharp peaks and specific profiles of powder XRD patterns.

Whereas celadonite and illite proper can be readily identified from a combination of XRD and chemical data, the overlapping ranges in cation composition and unit-cell parameters may complicate the differentiation of Al-glauconites and glauconites. Important additional information provided by FTIR spectroscopy allows not only unambiguous identification of Fe-bearing illites and celadonites, but also discriminates between glauconites and Al-glauconites and discriminates between illites proper and Fe-illites. In contrast, Fe-illites and Al-glauconites have similar FTIR characteristics, but have different ranges in cation composition and unit-cell parameters.

ACKNOWLEDGMENTS

B.B. Zviagina, V.A. Drits, and O.V. Dorzhieva acknowledge the financial support of the Federal Agency for Scientific Organizations (FANO Russia) budget project #0135-2016-0010, and T.A. Ivanovskaya, that of FANO Russia budget project #0135-2016-0021. Thanks are due to the anonymous reviewers for valuable comments.

REFERENCES

Bailey, S.W. (1980) Summary of recommendations of AIPEA nomenclature committee on clay minerals. *American Mineralogist*, **65**, 1–7.

Besson, G. and Drits, V.A. (1997a) Refined relationships between chemical composition of dioctahedral fine-dispersed mica minerals and their infrared spectra in the OH stretching region. Part I. Identification of the stretching bands. *Clays and Clay Minerals*, **45**, 158–169.

Besson, G. and Drits, V.A. (1997b) Refined relationship between chemical composition of dioctahedral fine-dispersed mica minerals and their infrared spectra in the OH stretching region. Part II. The main factors affecting OH vibration and quantitative analysis. *Clays and Clay Minerals*, **45**, 170–183.

Besson, G., Drits, V.A., Dayniak, L.G., and Smoliar, B.B. (1987) Analysis of cation distribution in dioctahedral micaceous minerals on the basis of IR spectroscopy data. *Clays and Clay Minerals*, **22**, 465–478.

Brigatti, M.F. and Guggenheim, S. (2002) Mica crystal chemistry and the influence of pressure, temperature and solid solution on atomistic models. Pp.1–97 in: *Micas: Crystal Chemistry and Metamorphic Petrology* (A. Mottana, F.E. Sassi, J.B. Thompson Jr. and S. Guggenheim, editors). Reviews in Mineralogy and Geochemistry, **46**, Mineralogical Society of America, Washington, D.C. with Accademia Nazionale dei Lincei, Roma, Italy.

Buckley, H.A., Bevan, J.C., Brown, K.M., Johnson, L.R., and Farmer, V.C. (1978) Glauconite and celadonite: two separate mineral species. *Mineralogical Magazine*, **42**, 373–382.

Dainyak, L.G., Rusakov, V.S., Sukhorukov, I.A., Zviagina, B.B., and Drits, V.A. (2009) An improved model for the interpretation of Mössbauer spectra of dioctahedral 2:1 *trans*-vacant Fe-rich micas: refinement of parameters. *European Journal of Mineralogy*, **21**, 995–1008.

Drits, V.A. (1987) *Electron Diffraction and High-Resolution Electron Microscopy of Mineral Structures*. Springer Verlag, Berlin.

Drits, V.A. (2003) Structural and chemical heterogeneity of layer silicates and clay minerals. *Clay Minerals*, **38**, 403–432.

Drits, V.A. and Kossovskaya, A.G. (1991) *Clay Minerals: Micas and Chlorites*. Nauka, Moscow, 175p. (in Russian).

Drits, V.A. and Zviagina, B.B. (2009) *Trans*-vacant and *cis*-vacant 2:1 layer silicates: structural features, identification and occurrence. *Clays and Clay Minerals*, **57**, 405–415.

Drits, V.A., Kameneva, M., Yu, Sakharov, B.A., Dainyak, L.G., Smoliar, B.B., Bookin, A.S., and Salyn, A.L. (1993b) *Problems in Determination of the Actual Crystal Structure of Glauconites and Related Phyllosilicates*. Nauka, Novosibirsk, 198p. (in Russian).

Drits, V.A., McCarty, D.K., and Zviagina, B.B. (2006) Crystal-chemical factors responsible for the distribution of octahedral cations over *trans*- and *cis*-sites in dioctahedral 2:1 layer silicates. *Clays and Clay Minerals*, **54**, 131–153.

Drits, V.A., Sakharov, B.A., Ivanovskaya, T.A., and Pokrovskaya, E.V. (2013) Crystal-chemical microheterogeneity of Precambrian globular dioctahedral mica minerals. *Lithology and Mineral Resources*, **48**, 503–528.

Drits, V.A., Weber, F., Salyn, A., and Tsipursky S.I. (1993a) X-ray identification of 1*M* illite varieties. *Clays and Clay Minerals*, **28**, 185–207.

Drits, V.A., Zviagina, B.B., McCarty, D.K., and Salyn, A.L. (2010) Factors responsible for crystal-chemical variations in the solid solutions from illite to aluminoceladonite and from glauconite to celadonite. *American Mineralogist*, **95**, 348–361.

Duplay, J. and Buatier, M. (1997) The problem of differentiating glauconite and celadonite. *Chemical Geology*, **84**, 264–266.

Farmer, V.C. (1974) The layer silicates. Pp. 331–363 in: *Infrared Spectra of Minerals* (V.C. Farmer, editor). Monograph 4, Mineralogical Society, London.

Ivanovskaya, T.A. (1994) Globular glauconite-illite layer silicates in Middle Riphean Debengdinsk Formation of the Olenek Uplift. *Lithology and Mineral Resources*, **29**, 595–605.

Ivanovskaya, T.A. (2009) Glauconitites in terrigenous rocks of the Khaipakh Formation (Middle Riphean, Olenek Uplift). *Lithology and Mineral Resources*, **44**, 348–366.

Ivanovskaya, T.A. and Tsipursky, S.I. (1990) First find of globular glauconite in the Lower Riphean, Anabar Uplift, *Litologia i Poleznye Iskopaemye*, **25**, no. 3, pp. 110–121 (in Russian).

Ivanovskaya, T.A., Tsipursky, S.I., and Yakovleva, O.V. (1989) Mineralogy of globular Riphean and Vendian layer silicates in Siberia and the Ural. *Lithology and Mineral Resources*, **24**, 271–284.

Ivanovskaya, T.A., Kats, A.G., Florova, Z.B., Tsipursky, S.I., and Yakovleva, O.V. (1993) Structure and lithomineralogical peculiarities of the Basal Lower Riphean in the Olenek Uplift (Osorkhayata Formation), *Stratigrafiya Geologicheskaya Korrelyatsiya*, **1**, 84–92 (in Russian).

Ivanovskaya, T.A., Gor'kova, N.V., Karpova, G.V., and Pokrovskaya, E.V. (2006) Layer silicates (glauconite, illite, chlorite) in terrigenous rocks of the Arymassi Formation (Olenek Uplift), *Lithology and Mineral Resources*, **41**, 601–623.

Ivanovskaya, T. A., Zaitseva, T. S., Zviagina, B. B., and Sakharov, B. A. (2012) Crystal-chemical peculiarities of globular layer silicates of the glauconite–illite composition (Upper Proterozoic, Northern Siberia). *Lithology and Mineral Resources*, **47**, 491–512.

Ivanovskaya, T. A. , Zviagina, B. B., Sakharov, B. A., Zaitseva, T. S., Pokrovskaya, E. V. and Dorzhieva. O. V. (2015) Globular layer silicates of the glauconite–illite composition in Upper Proterozoic and Lower Cambrian rocks. *Lithology and Mineral Resources*, **50**, 452–477.

Kimbara, K. and Shimoda, S. (1973) A ferric celadonite in amygdales of dolerite at Taiheizan, Akita prefecture, Japan, *Clay Science*, **4**, 143–150.

Lazarenko, E.K. and Pavlishin, V.I. (1976) Relationship of celadonite and svitalskite. in: *Mineralogy of Sedimentary Rocks*. 3. Naukova Dumka, Kiev (in Russian).

Longuépée, H. and Cousineau, P.A. (2006) Constraints on the genesis of ferrian illite and aluminum-rich glauconite: potential impact on sedimentology and isotopic studies. *The Canadian Mineralogist*, **44**, 967–980.

Madejova, J. (2003) FTIR techniques in clay mineral studies. *Vibrational Spectroscopy* **31**, 1–10.

Madejova, J. and Komadel, P. (2001) Baseline studies of The Clay Minerals Society Source Clays: Infrared methods. *Clays and Clay Minerals*, **49**, 410–432.

Malkova, K.M. (1956) On the celadonite of Pobuzhye. in: *Collected Papers on Mineralogy* **10**, 305–318, Lvov Geological Society, Lvov (in Russian).

Meunier, A. and El-Albani, A. (2006) The glauconite-Fe-illite-Fe-smectite problem: A critical review. *Terra Nova*, **19**, 95–104.

Muller, F., Drits, V.A., Plançon, A., and Besson, G. (2000) Dehydroxylation of Fe^{3+}, Mg-rich dioctahedral micas: (I) structural transformation. *Clay Minerals*, **35**, 491–504.

Murav'ev, V.I. (1983) *Mineral Parageneses of Glauconie-Siliceous Formations.* Nauka, Moscow, 208 pp. (in Russian).

Nikolaeva, I.V. (1977) *Minerals of the Glauconite Group in Sedimentary Formations*, Nauka, Novosibirsk, 319 pp. (in Russian).

Odom, I.E. (1984) Glauconite and celadonite minerals. Pp. 545–572 in: *Micas* (S.W. Bailey, editor). Reviews in Mineralogy, **13**, Mineralogical Society of America, Washington D.C.

Parron, C. and Amouric, M. (1990) Crystallochemical heterogeneity of glauconite and the related problem of glauconite-celadonite distinction. *Chemical Geology*, **84**, 286–289.

Rieder, M., Cavazzini, G., D'yakonov, Y.S., Frank-Kamenetskii, V.A., Gottardi, G., Guggenheim, S., Koval, P.V., Muller, G., Neiva, A.M.R., Radoslovich, E.W., Robert J.-L., Sassi, F.P., Takeda, H., Weiss, Z., and Wones, D.R. (1998) Nomenclature of the micas. *Clays and Clay Minerals*, **46**, 586–595.

Russell, J.D. and Fraser A.R. (1994) Infrared methods. Pp. 11–67 in: *Clay Mineralogy: Spectroscopic and Chemical Determinative Methods* (M.J. Wilson, editor). Chapman & Hall, London.

Sakharov, B.A. and Drits, V.A. (2018) Determination of small quantities of smectite layers in dioctahedral K-bearing micaceous minerals of illite, aluminoceladonite, and glauconite compositions. *Lithology and Mineral Resources*, **54** (in press).

Sakharov, B.A., Besson, G., Drits, V.A., Kameneva, M. Yu., Salyn, A.L., and Smoliar, B.B. (1990) X-ray study of the nature of stacking faults in the structure of glauconites. *Clay Minerals*, **25**, 419–435.

Shutov, V.D., Katz, M.Y., Drits, V.A., Sokolova, A.L., and Kazakov, G.A. (1975) Crystal chemistry of glauconites as an indicator of facial condition of their formation and postsedimentary transformation. Pp. 74–81 in: *Crystal Chemistry of Minerals and Geological Problems* (A.G. Kossovskaya, editor). Nauka, Moscow (in Russian).

Slonimskaya, M.V., Besson, G., Dainyak, L.G., Tchoubar, C., and Drits, V.A. (1986) Interpretation of the IR spectra of celadonites and glauconites in the region of OH-stretching frequencies. *Clay Minerals*, **21**, 377–388.

Środoń, J. and Eberl, D.D. (1984) Illite. Pp. 495-544 in: *Micas* (S.W. Bailey, editor). Reviews in Mineralogy, **13**, Mineralogical Society of America, Washington D.C.

Thompson, J.R. and Hower, J. (1975) The mineralogy of glauconite. *Clays and Clay Minerals*, **23**, 289–300.

Tóth, E. and Weiszburg, T. (2006) Two in one: Two different glauconite series from the same rock, Sümeg Marl Formation, Lower Cretaceous, Bakony Mountains, Hungary. P. 116 in: *Abstract Book/ 3rd Mid-European Clay Conference – MECC 06, Opatija, September 18-23, 2006* (I. Vlahović, D. Tibljaš, G. Durn, and V. Bišević, editors). Faculty of Science and Faculty of Mining, Geology and Petroleum Engineering, University of Zagreb.

Tsipursky, S.I. and Ivanovskaya, T.A. (1988) Crystal chemistry of globular layer silicates. *Litologiya i Poleznye Iskopayemye*, **23**, 41–49 (in Russian).

Velde, B. (1978) Infrared spectra of synthetic micas in the series muscovite-MgAl celadonite. *American Mineralogist*, **63**, 343–349.

Velde, B. (1985) *Clay Minerals: A Physico-chemical Explanation of Their Occurrence.* Developments in Sedimentology, **40**, Elsevier, Amsterdam.

Weiszburg, T., Tóth, E., and Beran, A. (2004) Celadonite, the 10-Å green clay mineral of the manganese carbonate ore, rkút, Hungary. *Acta Mineralogica-Petrographica*, **45/1**, 65–80.

Weiszburg, T., Tóth, E., and Pop, D. (2006) Continuous crystal-chemical space for the dioctahedral iron-rich micas and related phases (celadonite, glauconite, Fe-illite). P. 122 in: *Abstract Book/ 3rd Mid-European Clay Conference – MECC 06, Opatija, September 18-23, 2006* (I. Vlahović, D. Tibljaš, G. Durn, and V. Bišević, editors). Faculty of Science and Faculty of Mining, Geology and Petroleum Engineering, University of Zagreb.

Wilson, M.D. (2013) Rock-Forming Minerals, Volume 3C, Sheet Silicates: Clay Minerals., The Geological Society, London.

Zaitseva, T.S., Gorokhov, I.M., Ivanovskaya, T.A.,

Semikhatov, M.A., Kuznetsov, A.B., Mel'nikov, N.N., Arakelyants, M.M., and Yakovleva, O.V. (2008) Mössbauer characteristics, mineralogy and isotopic age (Rb–Sr, K–Ar) of Upper Riphean glauconites from the Uk Formation, the southern Urals, *Stratigraphy and Geological Correlation*, **14**, 227–247.

Zhukhlistov, A.P. (2005) Crystal structure of celadonite from the electron diffraction data. *Crystallography Reports*, **50**, 902–906.

Zviagina, B.B. and Drits V.A. (2012) Structural regularities in $2M_1$ dioctahedral micas: The structure modeling approach. *American Mineralogist*, **97**, 1939–1954

Zviagina, B.B., McCarty, D.K., Środoń, J., and Drits V.A. (2004): Interpretation of infrared spectra of dioctahedral smectites in the region of OH-stretching vibrations. *Clays and Clay Minerals*, **52**, 399–410.

Zviagina, B.B., Sakharov, B. A., and Drits V. A. (2007) X-ray diffraction criteria for the identification of *trans*- and *cis*-vacant varieties of dioctahedral micas. *Clays and Clay Minerals*, **55**, 467–480.

Zviagina, B.B., Drits, V.A., Środoń, J., McCarty, D.K., and Dorzhieva, O.V. (2015) The illite–aluminoceladonite series: Distinguishing features and identification criteria from X-ray diffraction and infrared spectroscopy data. *Clays and Clay Minerals*, **63**, 378–394.

(*Received 6 March 2017; revised 5 July 2017; Ms. 1169; AE: E. Ferrage*)